THE JOURNAL OF PHYSICAL CHEMISTRY C
A JOURNAL OF THE AMERICAN CHEMICAL SOCIETY

pubs.acs.org/JPCC

Article

Ternary Chalcogenide-Based Quantum Dots and Carbon Nanotubes: Establishing a Toolbox for Controlled Formation of Nanocomposites

Dominik Voigt,* Giulia Primavera, Holger Uphoff, Jan Alexander Rethmeier, Lukas Schepp, and Michael Bredol

Cite This: *J. Phys. Chem. C* 2022, 126, 9076–9090

Read Online

ACCESS | Metrics & More | Article Recommendations | Supporting Information

ABSTRACT: A general procedure based on electrostatic self-assembly for preparing nanocomposites based on carbon nanotubes (CNTs) and ternary chalcogenide semiconductor nanoparticles is shown. This was achieved by surface functionalization of the single components through well-established protocols, for CNTs, and a transferable general strategy for the nanoparticles. Heterostructures were then synthesized through electrostatic interaction between oppositely charged components. Structural, colloidal, and optical properties were characterized by transmission electron microscopy, X-ray diffraction, infrared spectroscopy, dynamic light scattering, ζ-potential, and absorption- and (time-resolved) photoluminescence measurements. Interestingly, the nanocomposites showed a blue shift in their excitation and emission spectra when compared to the pure nanoparticles but only when analyzed in powder form. Further investigations in the form of density functional theory (DFT) calculations were performed to evaluate the origin of the change in the optical properties.

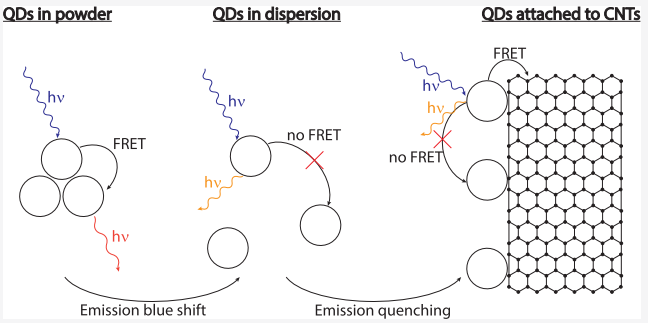

1. INTRODUCTION

Carbon nanotubes (CNTs), either in their single-walled (SWCNT) or multiwalled form (MWCNT), have gained a lot of attention in the past decades and established themselves in various scientific disciplines as well as in the fields of nanoengineering and nanotechnology,[1,2] such as nanomedicine,[3] electrode materials,[4−6] and optoelectronics.[7−9] The wide scope of applications is not surprising due to their exceptional characteristics. To name a few, some of the most prominent properties are their excellent thermal and electrical conductivity (owing to their delocalized π-electron system),[10] high Young's modulus[11] and tensile strength,[12] good resilience,[13] stability, and a high surface area.[14] Therefore, numerous studies have been conducted to modify and functionalize the sidewalls of the CNTs to expand their potential applications.[15−20]

Due to the high attention and research activity, the chemistry behind the functionalization of CNTs is well understood, which makes them together with their unique properties ideal candidates as templates for the assembly with other functional nanomaterials. It has been shown that the surface decoration of CNTs with various organic or inorganic species can increase the tunability of their physical, electrical, and optical properties.[21−23] Thus, as the demand for smaller, faster, and more efficient electronic devices increases, nanocomposites and functional CNTs with new or tuned properties may play an important role in the miniaturization process of nanoengineering and nanotechnology, including new catalyst materials,[24] sensitization of solar cells,[25] nanobatteries,[26] etc.

Within such applications, nanocomposites consisting of semiconductor quantum dots (QDs) that are attached to CNTs have emerged as an active field.[27−29] The unique possibility to tune important optical and electronic properties of the QDs by varying their size is of great interest in many applications.[30] Multinary chalcogenide materials, like $CuInS_2$ (CIS), $Cu(In,Ga)S_2$ (CIGS), and $Cu(In,Ga)Se_2$ (CIGSe) are herein of considerable interest as promising semiconductors for optoelectronic devices[31−33] due to their outstanding electronic and optical properties (owing to their properties as a direct band-gap semiconductor) and precise control of these by uncomplicated modification of the preparation conditions (size, surface chemistry, composition), as well as cost-efficient production out of commercially available precursors.

However, before nanomaterials can be efficiently utilized, there is the necessity to understand the synthesis, surface engineering, and internal effects, which can arise from the

Received: February 16, 2022
Revised: April 26, 2022
Published: May 23, 2022

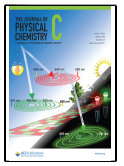

https://doi.org/10.1021/acs.jpcc.2c01142
J. Phys. Chem. C 2022, 126, 9076−9090

functionalization and combination of single nanomaterials into nanocomposites for their posterior integration and application. The aim of this work is, therefore, to investigate how, generally, QDs can chemically be attached to CNTs, what influence this has on the optoelectronic properties, and how they can be tuned through surface engineering. Based on our previous work that allows for versatile surface engineering of ternary chalcogenide-based nanocrystals[34] and well-established methods to functionalize the sidewalls of MWCNTs, we synthesized QD-CNT nanocomposites by simple electrostatic interaction for the present report. By modifying the surface with ligands of different alkyl chain lengths, the separation distance between QDs and CNT was varied and crucial properties such as the band gap and the electron transfer between the nanomaterials were studied intensively by experimental and theoretical ab initio methods.

2. METHODS

2.1. Chemicals and Reagents. MWCNTs (95% carbon assay, 6−9 nm × 5 μm (outer diameter × length)), ethylenediamine (EDA), *N*,*N*′-dicyclohexylcarbodiimid (DCC), copper(I) acetate (Cu(OAc)), indium(III) acetate ($In(OAc)_3$), zinc acetate ($Zn(OAc)_2$), stearic acid (SA), sulfur (S), 1-dodecanethiol (DDT), 1-octadecene (ODE), oleylamine (OAm), 8-amino-1-octanethiol-hydrochloride (AOT), 2-(dimethylamino)-ethanethiol hydrochloride (DMA), 2-(diethylamino)-ethanethiol hydrochloride (DEA), 3-mercaptopropionic acid (MPA), 11-mercaptoundecanoic acid (MUA), L-glutathione (L-GLU), and tetramethylammonium hydroxide (TMAH) were all purchased from Sigma Aldrich. Cysteamine hydrochloride (CYS), conc. nitric acid (HNO_3, w = 65%), chloroform ($CHCl_3$), *n*-hexane, methanol (MeOH), and toluene were obtained from Carl Roth. All reagents were used as received without any prior purification step.

2.2. Carboxyl Functionalization of Carbon Nanotubes (c-MWCNTs). Covalent carboxyl functionalized MWCNTs (c-MWCNTs) were obtained by partial oxidation with concentrated nitric acid similar to previous reports.[35] In a typical synthesis, 200 mg of pristine MWCNTs was dispersed in 60 mL of HNO_3 (w = 65%) and ultrasonicated for 30 min. Afterward, the mixture was heated up and refluxed for different oxidation times (2, 4, 6, and 8 h). Subsequently, the reaction was cooled to room temperature and the c-MWCNTs were purified by repeated centrifugation at 10,000 rpm for 15 min and washing with bidest. H_2O until the pH of the supernatant was neutral. The resulting solid was dried at 60 °C for 24 h. Stock solutions of c-MWCNT were prepared by dissolving them at concentrations of 0.5 mg/mL in bidest. H_2O by means of probe ultrasonication (at 20,000 kHz and a 48% amplitude for 3 min).

2.3. Amine Functionalization of Carbon Nanotubes (a-MWCNTs). Amine-functionalized MWCNTs (a-MWCNTs) were synthesized by covalent bonding of a diamine to the beforehand prepared c-MWCNTs with DCC, as described by Oytun et al.[36] In a typical synthesis, 10 mg of c-MWCNTs was dispersed in 10 mL of EDA and ultrasonicated for 30 min. Then, 350 mg of DCC was added and the mixture was sonicated for an additional 15 min. Afterward, the dispersion was stirred for 96 h at 100 °C temperature. For purification, the solution was centrifuged at 10,000 rpm for 15 min and washed with EtOH at least three times, and subsequent dried at 60 °C for 24 h. Stock solutions of a-MWCNT were prepared by dissolving them at concentrations of 0.5 mg/mL in bidest. H_2O by means of probe ultrasonication (at 20,000 kHz and a 48% amplitude for 3 min).

2.4. Synthesis of $CuInS_2$, $CuGaS_2$, and $CuInSe_2$ Core Quantum Dots. The synthetic approach was adopted from our previously published paper[34] and transferred from $CuInS_2$ (CIS) to synthesize $CuGaS_2$ (CGS) and $CuInSe_2$ (CISe). In a typical procedure, 73.5 mg (0.6 mmol) of Cu(OAc), 175.2 mg (0.6 mmol) of $In(OAc)_3$ (or 220.2 mg (0.6 mmol) $Ga(acac)_3$), 1023.9 mg (3.6 mmol) of SA, 15.0 mL of ODE, and 15.0 mL of DDT were loaded in a 50 mL three-neck flask and vacuumed for 30 min at 120 °C to remove any water or oxygen that was left in the reaction mixture. Afterward, it was flushed with Ar (by means of Schlenck-line technology) and heated with a heating mantle under vigorous stirring to 200 °C. Then, 2.4 mL of a solution prepared by dissolving 128.3 mg (4.0 mmol) of S in 10.0 mL of ODE at 120 °C (or 2.4 mL of a solution prepared by dissolving 315.8 mg (4.0 mmol) of Se powder in 5.0 mL of OAm and 5.0 mL of DDT at room temperature under a N_2 atmosphere) was injected quickly into the reaction mixture. The solution was further heated to 230 °C (240 °C for the synthesis of CGS) and kept at that temperature for 30 min to allow the growth of the core QDs. For the purification of the prepared nanocrystals, the reaction mixture was cooled to 60 °C with a water bath. Then, 10 mL of toluene was injected into the reaction mixture to stabilize the QDs. By adding MeOH, the QDs were precipitated and centrifuged at 10,000 rpm for 10 min. The supernatant was discarded and the underlying QDs were washed at least three more times with EtOH (T = 60 °C) to purify them. STEM photographs and the temporal evolution of the optical properties are shown in Figure S1a−f.

2.5. Synthesis of $CuInS_2$/ZnS, $CuGaS_2$/ZnS, and $CuInSe_2$/ZnS Core/Shell Quantum Dots. The growth of the first ZnS shell was carried out in situ directly after the completion of the QD core growth without any purification step. The reaction was quenched in an ice bath to temperatures of 60 °C and water-free $Zn(OAc)_2$ was added as a shell precursor. For details and the exact amount of $Zn(OAc)_2$ corresponding to a certain shell thickness, see the Supporting Information (Figure S2 and Table S1). The mixture was heated to 240 °C and held at that temperature for 2 h to let the ZnS shell grow around the nanoparticles. The purification of these core/shell QDs is similar to that of the core QDs.

2.6. Synthesis of $CuInS_2$/ZnS/ZnS, $CuGaS_2$/ZnS/ZnS, and $CuInSe_2$/ZnS/ZnS Core/Shell/Shell Quantum Dots. For the overgrowth of a second ZnS shell around the core/shell QDs to prepare core/shell/shell QDs, 0.3 mmol purified CIS/ZnS QDs were dissolved in 3.0 mL of $CHCl_3$ and placed together with 6.0 mL of OAm, 6.0 mL of ODE, and the amount of $Zn(OAc)_2$ needed for two more ZnS monolayers (ML) in a 50 mL three-neck flask. The flask was vacuumed at room temperature for 30 min. Afterward, it was flushed with Ar and heated with a heating mantle under vigorous magnetic stirring to 180 °C. Then, a stoichiometric amount of a solution prepared by dissolving 641.4 mg (20.0 mmol) of S in 20.0 mL of ODE at 120 °C was injected dropwise at a rate of 0.6 mL/min into the reaction system. After the addition of the S precursor, the second ZnS shell was allowed to grow for 2 h. Note: for CGS/ZnS/ZnS, an agglomerated turbid yellow/greenish solution was obtained instead of a clear and stable nanodispersion. Before purification, this mixture was centrifuged at 10,000 rpm for 5 min and the resulting clear yellow (luminescent) solution was processed further, while the green

https://doi.org/10.1021/acs.jpcc.2c01142
J. Phys. Chem. C 2022, 126, 9076−9090

solid residue was discarded (for a more detailed analysis of this observation, see Figure S4). Next, the reaction mixture was cooled to room temperature in a water bath and the CIS/ZnS/ZnS core/shell/shell QDs were precipitated by the addition of EtOH and centrifuged at 10,000 rpm for 5 min. The supernatant was discarded and the precipitate was redispersed in 5.0 mL of *n*-hexane and precipitated again by adding 10.0 mL of EtOH. This washing procedure was repeated at least three times.

2.7. Ligand Exchange. Further, 0.1 mmol core/shell/shell QDs were dissolved in 5.0 mL of $CHCl_3$. Under strong magnetic stirring, a solution of 2.0 mmol thiol (CYS, AOT, MPA or MUA) and 729.2 mg (4.0 mmol) of TMAH dissolved in 1.0 mL of MeOH was added dropwise. Afterward, the dispersion was stirred for 2 h. The mixture was precipitated at 10,000 rpm for 10 min and washed three times with 5.0 mL of bidest. H_2O and 30.0−40.0 mL of acetone. To ensure good long-term colloidal stability through a dense surface ligand coverage, the precipitate was dispersed in 5.0 mL of bidest. H_2O and 2.0 mmol corresponding thiol and refluxed for 2 h (for the MUA samples, this step was omitted because it led to irreversible agglomeration). The mixture was purified again as described above and dried at 50 °C for 24 h. Note: After drying, some samples could not be redispersed in an aqueous solution and formed turbid solutions. To yield clear and stable dispersions, 100 mg of core/shell/shell QDs and 100 mg of the corresponding thiol were refluxed once again for 1 h. The mixture was purified again as described above. During these clean-up steps, the colloidal stability increased with every washing step. Stock solutions of the QDs were prepared by dissolving a certain amount of nanocrystals in water to yield a 5.0 mg/mL concentration, adding the corresponding thiol as a stabilizer at concentrations of 1.0 mg/mL and adjusting the pH value of the solution with 1.0 mol/L HCl or NaOH depending on the nature of the stabilizing ligand (see Figure 3). Due to the nature of thiol ligands that oxidize quite rapidly, the stock solutions were stored in a fridge at 4 °C until further use. If agglomeration occurred after prolonged storage time, further addition of stabilizing ligands could redisperse the QDs, yielding clear solutions again.

2.8. QD-CNT Nanocomposite Synthesis. For the synthesis of QD-CNT composites, 50 mg core/shell/shell QDs (10.0 mL of the QD stock solution) and a certain amount of c-MWCNTs or a-MWCNT stock solution were added together (different nanocomposites with varying amounts of MWCNTs were prepared and the respective weight percentage (wt %) is with respect to the 50 mg of QDs) and filled up to 15.0 mL with bidest. H_2O. The pH of the solution is adjusted with 0.1−1.0 mol/L HCl or NaOH and afterward stirred for at least 3 h at room temperature. The resulting nanocomposites were analyzed in solution as well as in powder form after precipitation with EtOH and centrifugation at 10,000 rpm for 10 min and drying at room temperature for 24 h.

2.9. X-ray Diffraction (XRD) Analysis. The crystallographic structure of the prepared nanomaterials was studied by XRD techniques using a Rigaku MiniFlex II Desktop diffractometer equipped with a radiation source from an X-ray tube with Cu Kα radiation (λ = 1.54 Å). Measurements were performed in a 2θ range of 20−80° with a scan rate of 2°/min and 0.02° increases.

2.10. Size and ζ-Potential Measurements. A Malvern Instruments Zetasizer Nano ZS was used for particle size determination by dynamic light scattering (DLS) and ζ-potential from electrophoretic mobility measurements, together with a standard pH meter (SevenMulti, Mettler Toledo). Measurements were performed from sample dispersions of 0.1−5 mg/mL. The pH value was varied using hydrochloric acid (0.1−1.0 M) and sodium hydroxide (0.1−1.0 M). For DLS measurements, a 633 nm laser in combination with 173° backscatter detection was used. Each measurement was averaged from 10 runs, each lasting 10 s. The measurements were repeated three times and the averages were taken. For the ζ-potential, each measurement was collected from 15 runs; all experiments were repeated three times and the averages were recorded.

2.11. Photoluminescence (PL), PL Decay, and Absorption Measurements. PL and absorption spectra as well as PL decay curves at room temperature were recorded to characterize the optical properties. Emission spectra were recorded using a Spectrofluorophotometer FS5 from Edinburgh Instruments. UV−vis absorbance measurements were performed using an Analytik Jena Specord 200Plus. PL decay curves were measured on a fluorescence spectrometer FLS980 from Edinburg Instruments, equipped with an EPL-450 ps laser (λ_{ex} = 445.6 nm, pulse width ≤ 70 ps). For the measurements of the decay curves, the monitoring wavelength was set to the wavelength of the PL at its maximum intensity.

2.12. Cyclic Voltammetry (CV) and Differential Pulse Voltammetry (DPV). A ModulLabXM ECS from Solartron analytical was used for the electrochemical characterization of the samples. Measurements were performed in a three-electrode cell using a 1 cm^2 platinum sheet counter electrode (CE), a silver wire pseudo reference electrode (RE), and a 3 mm (diameter) glassy carbon (GC) working electrode (WE). The RE is calibrated against the ferrocene/ferrocenium (Fc/Fc+) couple.[37] $LiClO_4$ (0.1 M) in acetonitrile (CH_3CN) was used as an electrolyte. CV tests were performed in the electrolyte with a potential of +1.5 to −2.0 V (relative to the ferrocene (II/III) standard reduction potential) at a scan rate of 100 mV/s. DPV measurements were carried out with an increasing potential of 3 mV, a pulse amplitude of 60 mV, a pulse width of 50 ms, and a pulse period of 500 ms. To perform measurements on the QD/MWCNT composites, the GC working electrode was dip-coated with a thin film of the sample material. To increase the affinity of the QDs to the electrode and to improve the accuracy of the coating, the GC substrate underwent a number of cleaning and preparation steps: polishing with a 0.3 μm alumina slurry on paper cloth for 2 min, rinsing with deionized water, cleaning in an ultrasonic bath with deionized water for 15 min followed by pure ethanol for 10 min, and then drying in air. The clean and pretreated substrate was dipped into a water-based dispersion of the QD/MWCNT for 20 min, then air-dried. The procedure is repeated twice for each sample.

2.13. Fourier Transform Infrared (FTIR) Spectroscopy. The adsorption of organic ligands and capping of the nanoparticles were studied by FTIR spectroscopy using a Nicolet iS 5 with a diamond attenuated total reflectance (ATR) controller from Thermo Fischer Scientific. Measurements were performed from 4000 to 600 cm^{-1}.

2.14. Computational Details. Calculations were performed in the framework of a density functional theory (DFT) computational method,[38,39] as implemented in the Quantum ESPRESSO package.[40,41] Energies were calculated using a plane-wave basis set, scalar relativistic ultrasoft pseudopotentials (USPP), and the generalized gradient approximation

https://doi.org/10.1021/acs.jpcc.2c01142
J. Phys. Chem. C 2022, 126, 9076−9090

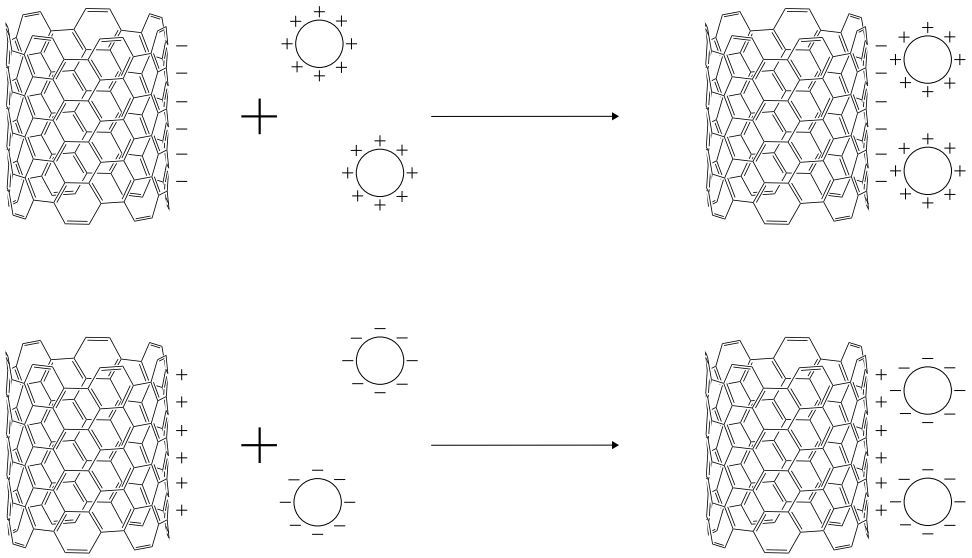

Figure 1. Illustration of the preparation of QD/MWCNT heterostructures by electrostatic self-assembly.

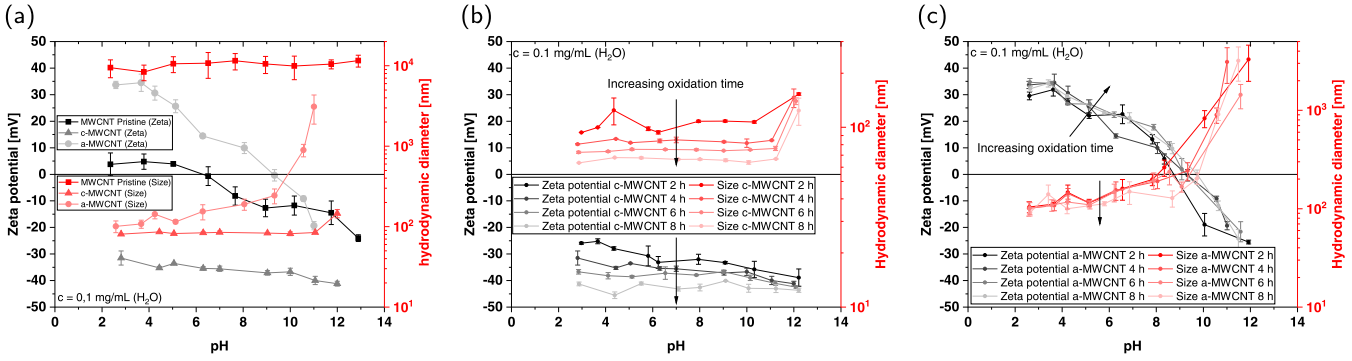

Figure 2. ζ-Potential and DLS size dependency on the pH value of pristine MWCNTs (a), c-MWCNTs (b), and a-MWCNTs (c).

(GGA) with the Perdew–Burke–Ernzerhof (PBE) functional to describe the exchange–correlation potential.[42] To improve the accuracy of the calculations, a Hubbard U correction[43] was applied on the Cu 3d, Ga 3d, In 4d, Zn 3d, S 2p, and Se 3 3p states to correct the well-known problem that LDA and GGA functionals underestimate the band gap and are not able to reproduce the correct position of d or f states of transition or rare earth metals.[44] Since the linear-response theory (used to calculate ab initio values for the Hubbard U parameters[45]) has its limitations and fails for closed-shell systems,[46] the U parameters were optimized simultaneously to reproduce the experimental lattice parameter, band gap, and the relative position of d states of ZnS and $CuInS_2$, similar to Mattioli et al. and Khan et al.[47,48] Satisfactorily converged results were achieved using 60 Ry as the kinetic energy cutoff for wave functions and 480 Ry as the kinetic energy cutoff for the charge density and potential (see Figure S11). The convergence thresholds for selfconsistency, the total energy, the forces for ionic minimization, and the pressure for variable cell relaxations were set at 1.0×10^{-8} Ry, 1.0×10^{-4} Ry, 1.0×10^{-3} Ry/Bohr, and 5.0×10^{-4} GPa, respectively. A $6 \times 6 \times 6$ Monkhorst–Pack k-point grid including the Γ point was used for sampling the 1st Brillouin zone of bulk ZnS, $CuInSe_2$, $CuInS_2$, and $CuGaS_2$, while a Γ-point-only sampling was used for the calculation of the stand-alone QDs and CNT-QD structures. The supercell with the QD located at the center contains a vacuum region of at least 10 Å to avoid periodic interactions. Furthermore, to compensate for surface defect states arising from dangling bonds on surface ions, pseudoatoms, with fractional nuclear charges (1.75 for Cu^+, 1.25 for In^{3+} and Ga^{3+}, 1.5 for Zn^{2+}, and 0.5 for S^{2-} and Se^{2-}) as suggested by Huang et al.,[49] were used to passivate these. Electronic band and state positions with respect to the vacuum level were obtained by calculating the planar average electrostatic potentials along the z-axis and the vacuum region was used as the absolute energy reference. The QDs were constructed by cutting out a spherical shape from the optimized underlying bulk structure by selecting all atoms within a radius of $r < x^2 + y^2 + z^2$ around a sulfur atom. All systems were optimized with respect to their geometry before any electronic structure calculation was performed.

3. RESULTS AND DISCUSSION

3.1. Surface Modification of MWCNTs. The synthetic strategy, illustrated in Figure 1, for the construction of nanocomposites consisting of QDs and MWCNTs follows electrostatic self-assembly of the single components. This can be achieved by electrostatic interaction between charged functional groups (i.e., protonated amine groups and deprotonated carboxyl groups). The main advantage of this approach is that important properties like, e.g., band gaps and band edges can be fine-tuned before the building blocks of the composite are united. Thus, already established and well-

https://doi.org/10.1021/acs.jpcc.2c01142
J. Phys. Chem. C 2022, 126, 9076–9090

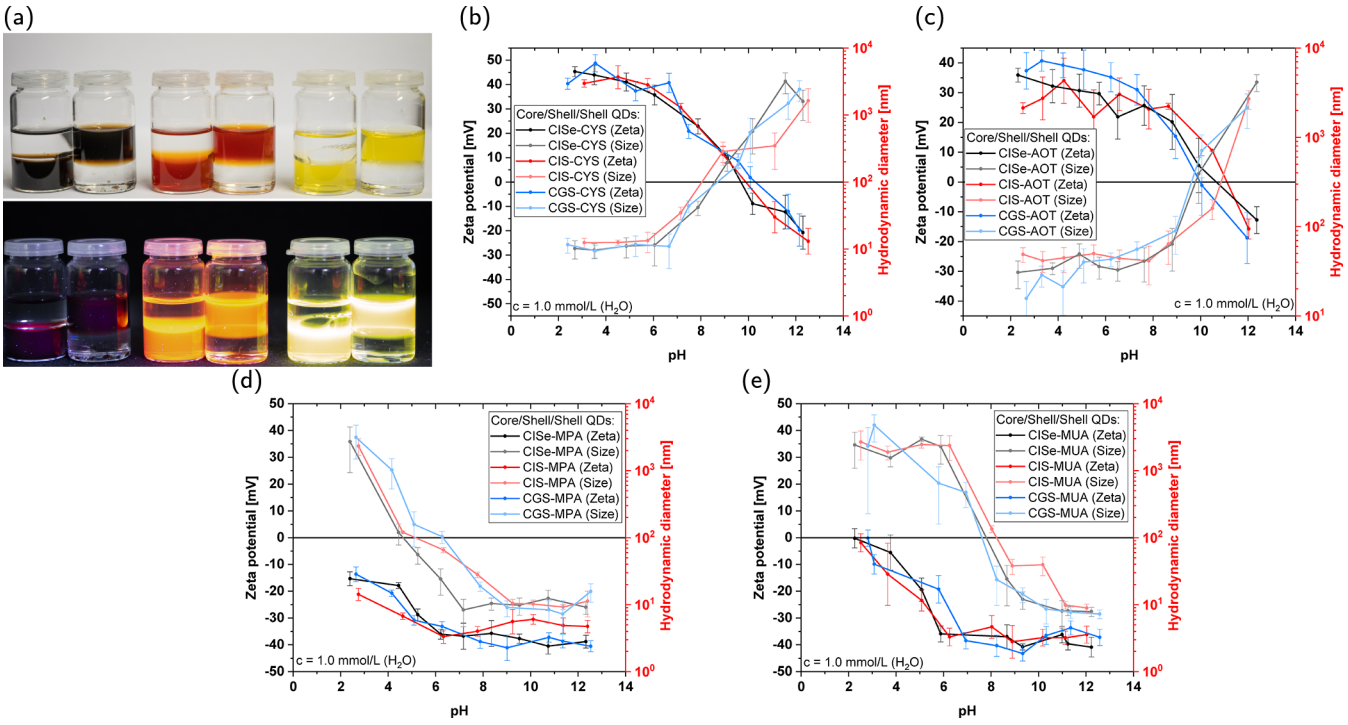

Figure 3. Photographs of the phase transfer from organic to aqueous media under daylight and UV light (a), ζ-potential and DLS size dependency of the pH value of CYS- (b), AOT- (c), MPA- (d), and MUA- (e) capped CISe, CIS, and CGS QDs.

controlled synthesis protocols can be used. To yield charged CNTs, the pristine MWCNTs were functionalized and carboxyl and amino groups were introduced to the sidewalls (c-MWCNT and a-MWCNT). In Figure 2a, the pH-dependent ζ-potential and DLS size curves of pristine MWCNTs are shown and what happens after carboxylation and amidation (c-MWCNT and a-MWCNT). Pristine MWCNT without any functional groups on the surface are not colloidally stable, as indicated by high hydrodynamic diameters (agglomerates). After oxidative treatment by boiling the pristine MWCNT in concentrated nitric acid, the partial oxidation from pristine CNTs to c-MWCNT leads to carboxyl groups on the nanotube surface; these can easily be deprotonated, resulting in a negative surface charge and repulsion between single nanotubes[50] thus yielding stable dispersions in water over a large pH range. By increasing the oxidation time, more functional groups are introduced, and simultaneously more of the structure gets altered and destroyed.[51] As it can be seen, the ζ-potential as well as the hydrodynamic diameter are decreasing (see Figure 2b). Also, visible damages on the sidewalls were observed for prolonged oxidation times (see Figure S7). After amidation of the c-MWCNT to a-MWCNT, mostly amine groups are the functional groups on the outer sidewalls. These can be protonated in acidic conditions resulting in positive surface charges, leading again to repulsion between the nanotubes and stable dispersions. But different from c-MWCNT, the colloidal stability of a-MWCNT is given in a smaller pH range. Above pH ∼9.5, the surface charges are not high enough to compensate for the intermolecular forces and agglomeration occurs, which is in accordance with increasing hydrodynamic diameters (see Figure 2c). Using c-MWCNT with more functional carboxyl groups to synthesize a-MWCNT (longer oxidation times) should also lead to more amine groups and thus to higher positive surface charges. This is why the trend of the ζ-potential is reversed with oxidation time, as indicated by the arrows. However, the influence on the ζ-potential and DLS sizes is not that pronounced as it is for c-MWCNTs, but still a trend toward higher ζ-potentials and a wider pH range of colloidal stability is observed.

3.2. Synthesis and Surface Engineering of CIS-, CGS-, and CISe-Based QDs. To obtain charged nanocrystals based on $CuInS_2$, $CuGaS_2$, and $CuInSe_2$, our previously published work for the versatile surface engineering of QDs[34] was used as a fundament and further developed. As shown in Figure S5a, the XRD diffraction peaks reveal that the synthesis protocol can be easily modified to synthesize different chalcopyrite nanometer-sized materials. All diffraction peaks are broadened due to the finite particle size,[52] which is in accordance with STEM photographs of core/shell nanoparticles with different shell thicknesses (see Figure S3a−c). Figure S5a,b shows the absorption and emission spectra of these three chalcopyrite materials as well as photographs. Due to differences in the band gaps of the materials, the emission peaks and absorption bands are blue-shifted from $CuInSe_2$ over $CuInS_2$ toward $CuGaS_2$, which is in accordance with the literature,[53] emphasizing again that the modified synthesis protocol works. Also shown is the influence of the passivating ZnS shell. With an increase of ZnS monolayers (ML) around the QD cores, the photoluminescence intensity increases substantially and blue shifts toward higher energies. The intensity increase can be attributed to the quenching of surface and trap states and the blue shift is a result of the QD cores shrinking[54] and the formation of ZnS alloyed cores through diffusion and cation exchange processes.[55]

The results of the ligand exchange are shown in Figure 3. Photographs show the success of the phase transfer from organic to aqueous media with only minor influences on the optical properties (see Figure 3a). Confirmation of the replacement of oleylamine as a capping ligand with different

https://doi.org/10.1021/acs.jpcc.2c01142
J. Phys. Chem. C 2022, 126, 9076−9090

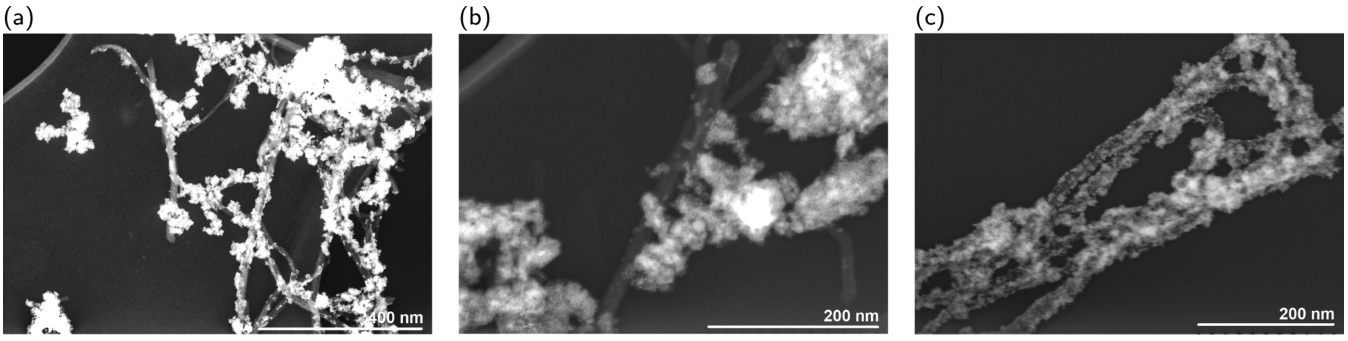

Figure 4. STEM photographs of differently prepared nanocomposites: oppositely charged QDs and MWCNTs but an unstable pH region (a), equally charged binary components and a stable pH region (b), and oppositely charged building blocks and a stable pH region (c).

thiol-based ligands is presented via the pH-dependent ζ-potentials and DLS sizes (Figure 3b−e). For CYS- and AOT-capped nanoparticles, high positive ζ-potentials were measured in acidic media, yielding stable dispersions as indicated by low hydrodynamic diameters. CYS and AOT molecules possess a functional amine group, which can be easily protonated (and positively charged) at low pH values, explaining the measured positive ζ-potential. The charged particles repulse each other through Coulombic forces, which is in accordance with the observed stable dispersions and low measured particle sizes. With an increase in the pH value, the ζ-potential decreases ($-NH_3^+$ deprotonates and loses the charge), the dispersions become unstable, and the QDs start to agglomerate as it is pointed out with measured increasing DLS sizes (electrostatic repulsion between particles gets weakened so much that attracting intermolecular forces like dipole−dipole, hydrogen bonds, and van der Waals interactions are dominating). For MPA- and MUA-capped QDs, the trend is reversed, indicating that high negative ζ-potentials were measured in basic media leading to stable dispersions and small hydrodynamic diameters. On decreasing the pH (and therefore the absolute value of the ζ-potential), agglomerates were formed, again indicated by increased measured particle sizes. The functional group in MPA and MUA molecules is a carboxyl group, which can be easily deprotonated in basic media leading to a negative charge and electrostatic repulsion between particles capped with these ligands. Similar to described above, when the carboxyl group loses its charge (e.g., gets protonated at lower pH values), the dispersion loses stability and agglomerates are observed. A further indication of a successful ligand exchange is the FTIR spectra presented in Figure S6 with the most characteristic absorption bands (like the stretching vibration of COOH, C═O, C−O, N−H, and C−N) together with adsorbed water.

To our best knowledge, this is the first report of $CuInSe_2$- and $CuGaS_2$-based nanocrystals capped with cysteamine and $CuInSe_2$, $CuInS_2$, and $CuGaS_2$ capped with 8-amino-1-octanethiol as a ligand, once again highlighting the possibility of universally changing the surface properties of chalcopyrite nanomaterials, and thus generating a toolbox for the construction and design of new heterostructures in the nanometer region.

3.3. Electrostatic Interaction between QDs and MWCNTs to Form Nanocomposites. A prerequisite for the formation of QD/MWCNT nanocomposites is that the single building blocks are colloidally stable and sufficiently charged. The above described and characterized surface functionalization of both MWCNTs and QDs reveals that c-MWCNTs are negatively charged and colloidally stable over the whole measured pH range (see Figure 2b, from pH ∼2.5−12.0). Oppositely charged QDs (functionalized with CYS or AOT) were stable from about pH ∼2.5−8 (see Figure 3b,c). Thus, for the synthesis of heterostructures consisting of negatively charged MWCNTs and positively charged QDs, a wide pH range could be utilized. Unlike c-MWCNTs, a-MWCNTs, which are positively charged were only stable till a pH of ∼9.5, above which agglomeration occurred (see Figure 2c). Negatively charged QDs (functionalized with MPA or MUA) were only stable above pH ∼8.5 (see Figure 3d,e). This together gives a very small pH window for the preparation of nanocomposites consisting of positively charged MWCNTs and negatively charged QDs.

In Figure 4, this is illustrated with STEM photographs of nanocomposites prepared under different conditions. It can be seen that if equally charged QDs and MWCNTs in stable conditions or oppositely charged binary components but in unstable conditions (in terms of the above-discussed pH value) were used to prepare QD/MWCNT heterostructures a bad, up to nonexistent surface coverage of the carbon nanotube sidewalls with nanoparticles was observed (as it can be seen in Figure 4a,b). In contrast, if oppositely charged QDs and MWCNTs in stable conditions were used to prepare the nanocomposites, a fine homogeneous and even decoration and coverage of the MWCNTs surface with QDs were achieved (Figure 4c). This highlights the above-mentioned necessity that the single components used for the synthesis need to be colloidally stable and also underlines the precise control of the electrostatic interaction via the pH of the solution. For an overview and zoomed-in STEM photographs, see Figure S9. In areas where multiple nanotubes overlap each other, a clustering of the nanoparticles is observed, which is in accordance with previously observed bridging adsorption between multiple CNTs by the charged nanoparticles.[56] Differences for composites prepared with low or high concentrations of MWCNTs or with core/shell nanoparticles with thin or thick shells can be seen in Figure S10. It should be noted, however, that the reversing of the self-assembly could not be achieved by varying the pH value. For that to happen, repulsive forces between the components would be necessary, which means one of the components has to switch its surface charge from negative to positive or vice versa. As was indicated via the pH-dependent ζ-potentials and particle sizes above, the components are only colloidally stable in acidic or basic media (not in both, except the c-MWCNT, but they possess a negative ζ-potential across all measured pH values), indicating that agglomerates would form when one tries to invert the

https://doi.org/10.1021/acs.jpcc.2c01142
J. Phys. Chem. C 2022, 126, 9076−9090

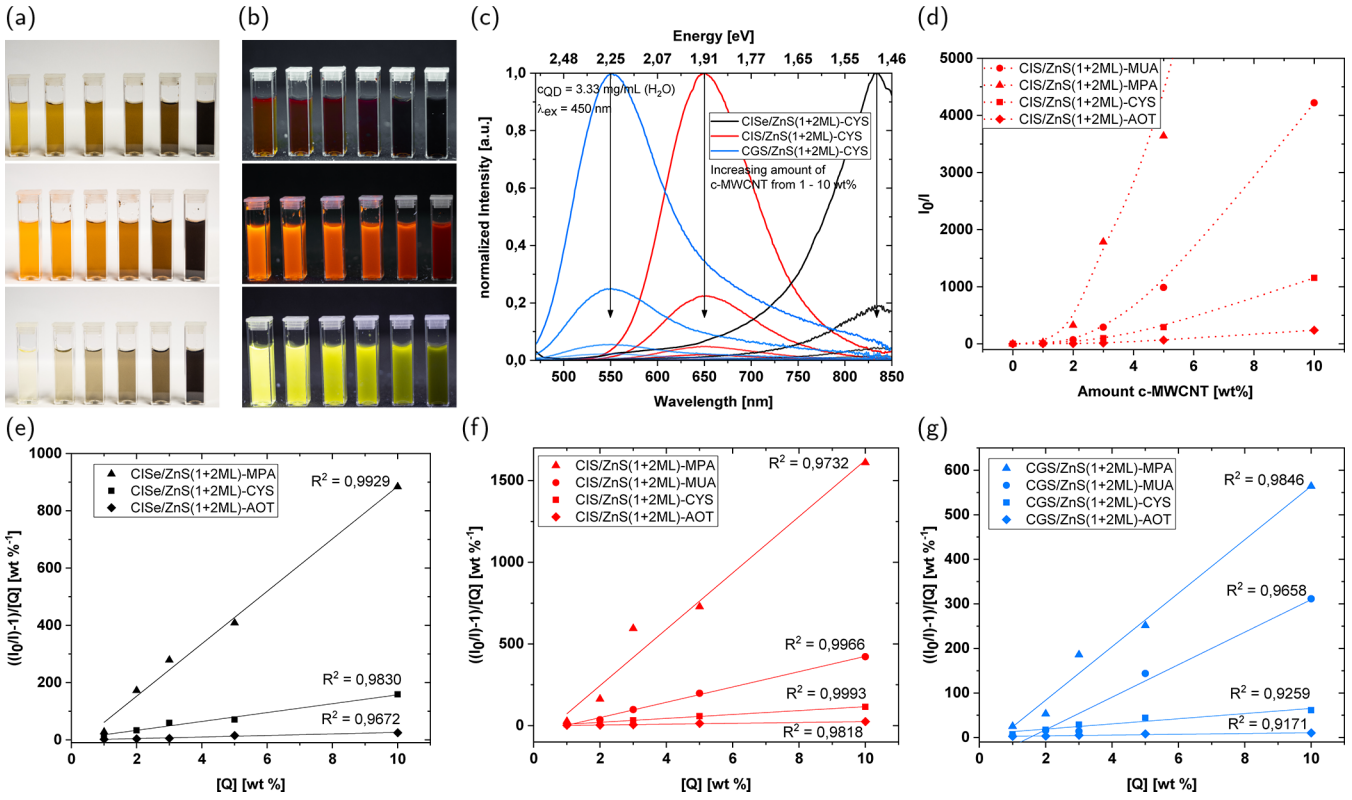

Figure 5. Optical appearance of the composites with different amounts of CNTs under daylight (a) and UV light (b) (345 nm excitation); corresponding emission spectra (c); Stern−Volmer plot for only dynamic quenching of CIS-CNT composites (d); and Stern−Volmer plots for both dynamic and static quenching of CISe-CNT (e), CIS-CNT (f), and CGS-CNT (g) heterostructures.

surface charge via the pH. When agglomerates are observed, it is a sign that the attractive forces are stronger than the repulsive ones. However, in theory, such a composite with reversible self-assembly could be produced with bifunctional (zwitterionic) components and might be an interesting topic for further research.

Further investigations were carried out to examine the optical properties of the synthesized nanocomposites by photoluminescence emission and excitation spectroscopy (for simplicity and clarity, only the emission spectra are shown here; the excitation spectra are shown in Figure S8a). Figure 5a,b shows the optical appearance of cysteamine-capped $CuInSe_2$, $CuInS_2$, and $CuGaS_2$ (from top to bottom)-based nanoparticles without and with 1, 2, 3, 5, and 10 wt % c-MWCNTs (from left to right) as stable dispersions. Figure 5c shows the corresponding emission spectra, showing the characteristic broad peaks in the near-infrared region for CISe, around 650 nm for CIS and around 550 nm for CGS. Luminescence quenching is observed with the addition of the nanotubes. This has two possible reasons. As carbon nanotubes are an absolute black material, they obviously absorb light in the visible up to the near-infrared region of the electromagnetic spectrum.[57] Furthermore, a nonradiative decay pathway, resulting from a charge transfer of photoexcited electrons or holes from the conduction or valence band of the nanocrystals (donor) to the empty electronic states of the CNTs (acceptor) is possible.[58] Such a charge transfer should only be possible when the separation distance between MWCNTs and QDs is small, indicating a strong attachment between the components (such behavior was observed above, as shown in Figure 4c). Further investigations of the charge transfer were performed in terms of Stern−Volmer analysis.[59] As shown in Figure 5d, the Stern−Volmer plot of CIS-based nanoparticles capped with different ligands gave nonlinear behavior. A possible reason for these nanocomposites to give nonlinear Stern−Volmer plots is the presence of both static and dynamic quenching.[60] This would mean that the standard expression of the Stern−Volmer equation is given as follows

$$\frac{I_0}{I} = 1 + K_d[Q] \tag{1}$$

where I_0 and I are the intensity maximum of the unquenched and quenched emitter, [Q] is the concentration of the quencher, and K_d is the Stern−Volmer constant that in a purely dynamic fluorescence quenching process is the product of the bimolecular quenching rate constant and the fluorescence lifetime in the absence of an added quencher, which gets modified by a second term responsible for the static fluorescence quenching process to give the following expression

$$\frac{I_0}{I} = (1 + K_d[Q])(1 + K_s[Q]) \tag{2}$$

$$\left(\frac{I_0}{I} - 1\right)\frac{1}{[Q]} = (K_d + K_s) + K_dK_s[Q] \tag{3}$$

where K_s is the Stern−Volmer constant in a purely static fluorescence quenching process. Figure 5e−g shows the Stern−Volmer plots for simultaneous static and dynamic fluorescence quenching. It can be seen that after linear fitting and regression analysis, the data points and calculated R^2 values almost show a linear behavior. As luminescence

https://doi.org/10.1021/acs.jpcc.2c01142
J. Phys. Chem. C 2022, 126, 9076−9090

quenching through charge transfer is a way more complex topic as we represented it here, there are a lot more reasons for nonlinear Stern−Volmer plots, explaining the still not ideal R^2 values. Nevertheless, the simplified representation is sufficient for our intents and characterization. The quenching rates for longer chain ligands decrease, as can be seen when comparing MPA- and MUA-capped (or CYS and AOT capped) quantum dots, which can be attributed to hindered charge transfer of the photoexcited exciton from the semiconductor material to the MWCNTs due to elongated separation through the ligand. This is in accordance with previous reports.[61] However, the length of the ligand is not the only variable responsible for the charge transfer, as negatively charged QDs have much higher quenching rates than positively charged QDs (despite, e.g., CYS being a shorter ligand than MUA). This suggests an overall stronger interaction between negatively charged QDs and a-MWCNTs than between positively charged QDs and c-MWCNTs, as it is also described by Pan et al.[62] It is further indicated that next to static quenching, dynamic quenching is present through PL decay lifetime measurement.[63] If the lifetime values remain unchanged in the presence of MWCNTs, it might be due to static quenching. However, as shown in Figure 6, there was a decrease in lifetime with increasing amount of nanotubes, which supports our assumption of both static and dynamic luminescence quenching being present.

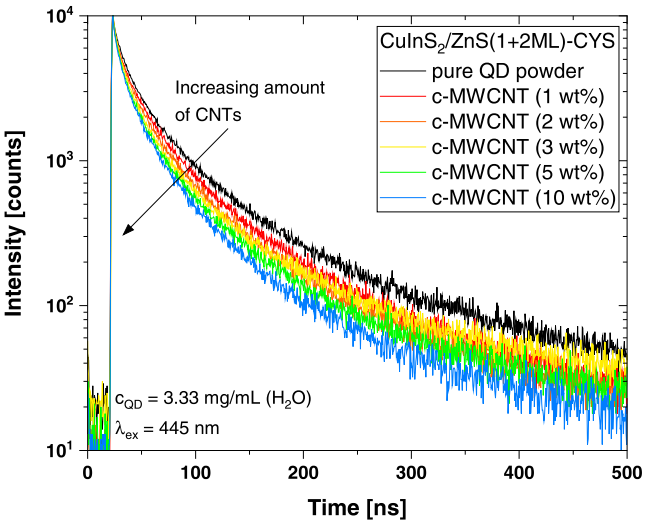

Figure 6. PL decay times of cysteamine-capped CIS-based QDs with increasing amounts of c-MWCNTs.

Another interesting finding was that when the dispersed nanocomposites were precipitated, dried, and analyzed in their powder form, a slight blue shift of ∼10−20 nm of the emission peak was observed when heterostructures were compared to the pure QDs (also after precipitation in powder form), as shown in Figure 7. This behavior was observed for all used semiconductor materials, and in Figure 8a−d, it can be seen that it is also independent of the capping ligand. Interesting to mention is that the emission maximum of the composite materials is almost at the same wavelength as the emission maximum of the quantum dots in solution. Also, it should be noted that no blue shift was observed for the dispersed nanocomposites in solution or for powder nanocomposites prepared from unstable conditions, as shown in Figure S8b,c.

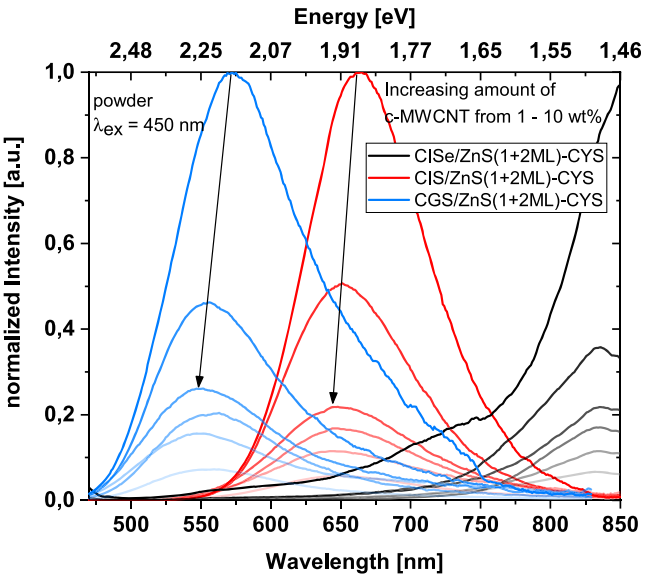

Figure 7. Emission spectra of cysteamine-capped CISe-, CIS-, and CGS-based QDs with increasing amounts of c-MWCNTs, characterized in their powder form.

Further, no shifts were observed from electrochemical analysis, as shown in Figure 9. The cathodic DPV peak voltage increases toward higher negative potentials from CISe over CIS toward CGS (Figure 9a) and upon increasing the thickness of the ZnS shell (Figure 9b). Only the cathodic reduction peak was observable, as the anodic oxidation of the nanoparticles is at higher potentials than that of the GC working electrode (see the CV scan). Nevertheless, the cathodic peak contains information about the conduction band minimum (CBM),[64] which upon increasing the band gap also has to shift toward higher energies. For the composite material, the intensity of the peak voltage increases upon increasing the amount of MWCNTs, which is the result of higher conductivities in those samples, but a shift of the peak voltage, as was observed for different semiconductor materials or thicker shells, did not occur. This indicates that the observed blue shift is an optical phenomenon rather than an influence on the electronic structure of the semiconductor material. However, optical observations are reported for nanoparticles attached to the sidewalls of carbon nanotubes or other substrates[56,65−67] and explained by electrostatic interactions between the binary components and the influence of electric fields originating from the substrate onto the band gap of the semiconductor material (quantum-confined stark effect).

To test this assumption, we compared nanocomposites constructed from cysteamine-capped CIS/ZnS QDs and c-MWCNTs that were functionalized for different times by partial oxidation through boiling in concentrated nitric acid. As it was discussed above, this led to more functional groups and thus to more charges and stronger electric fields (see Figure 2b). If the electric fields would be responsible for the observed blue shift, we would expect a trend with increasing the electric field. However, this is not what we measured, as shown in Figure 10a,b. The emission maximum of the heterostructures is at almost the exact wavelength, slightly shifted by ∼20 nm compared to the pure QDs. This observation suggests that the electrical field exerted from the substrate might not be the reason for this shift. Further investigations and discussions about the origin of this shift will follow in the next section (see

https://doi.org/10.1021/acs.jpcc.2c01142
J. Phys. Chem. C 2022, 126, 9076−9090

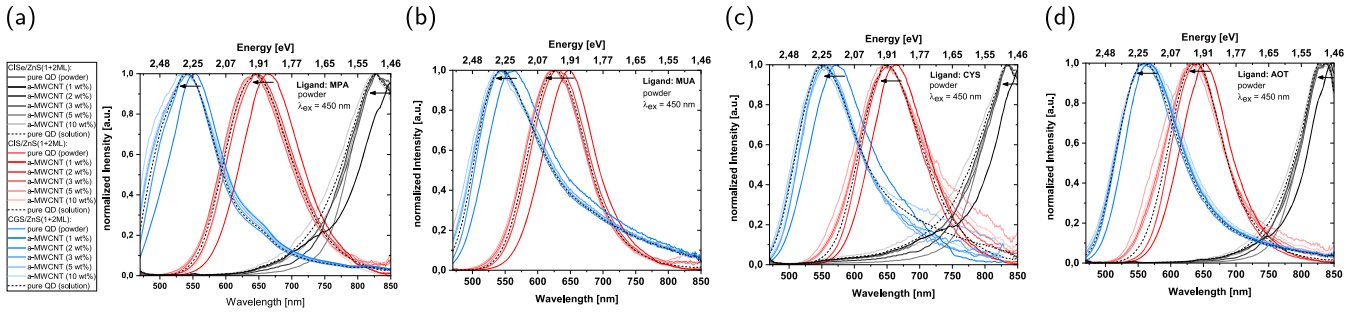

Figure 8. Normalized emission spectra of MPA- (a), MUA- (b), CYS- (c), and AOT- (d) capped nanoparticles based on CISe, CIS, and CGS, characterized in their powder form and compared to emitters in solution.

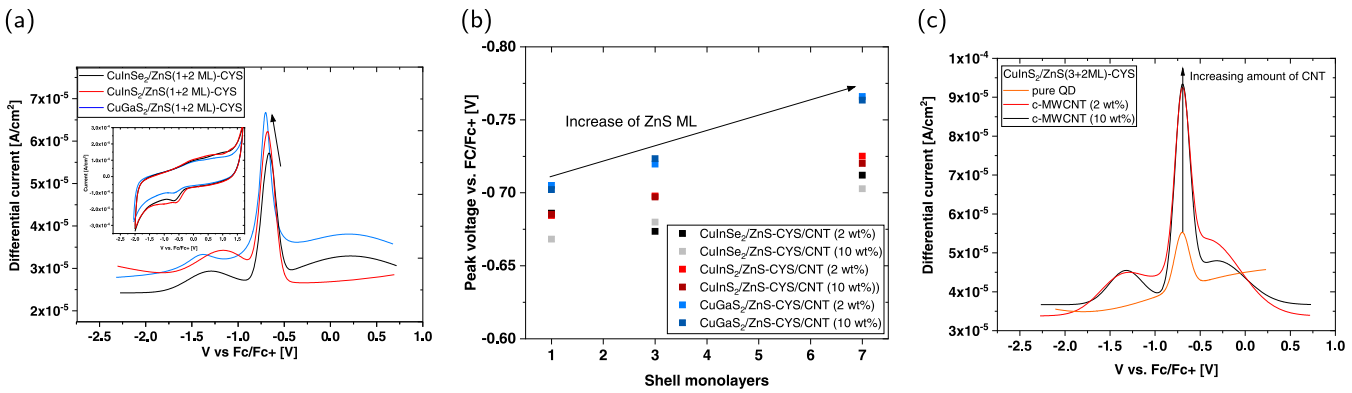

Figure 9. Comparison of cathodic DPV scans of different chalcogenide core/shell nanoparticles (a) (inset shows the CV scan), DPV scans of pristine cysteamine-capped $CuInS_2$/ZnS core/shell nanoparticles and attached to c-MWCNTs (b), and DPV peak voltage of CISe, CIS, and CGS QD/MWCNT structures with increasing amounts of ZnS monolayer shells (c).

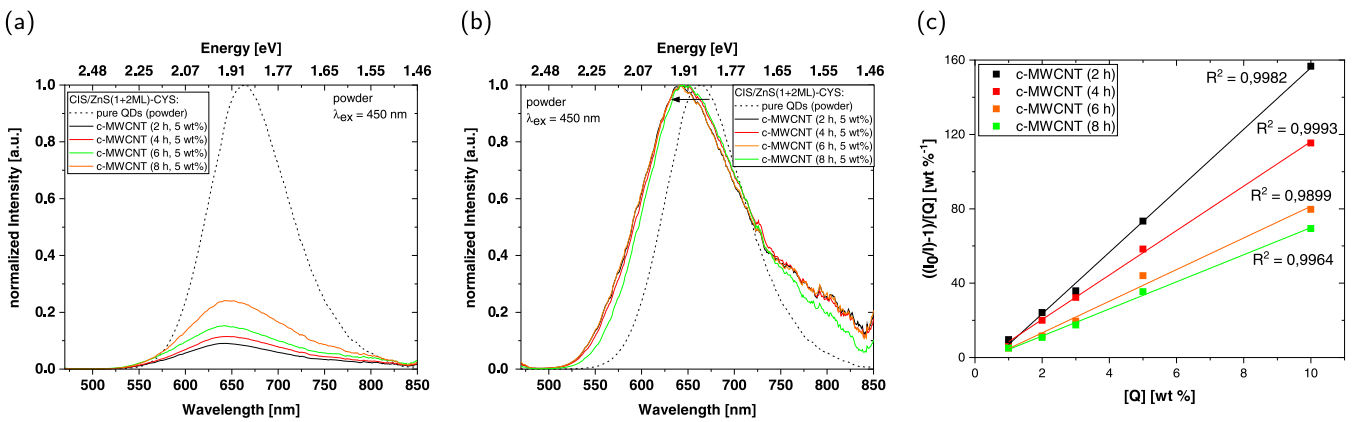

Figure 10. Normalized emission spectra of heterostructures constructed from cysteamine-capped $CuInS_2$/ZnS nanoparticles and c-MWCNT with different oxidation times (a, b) and the corresponding Stern−Volmer plots (c).

Section 3.4). Figure 10c shows the corresponding Stern−Volmer plots showing that an increase in oxidation time leads to reduced photoluminescence quenching. This can be attributed to the partial destruction of the conjugated π-electron system when oxidizing the scaffold of the nanotubes to introduce −OH, −CHO, and −COOH groups, and by destroying this delocalized electron system, the ability to act as a charge acceptor gets additionally weakened.[68] Furthermore, the influence of the shell thickness on quenching rates and charge transfer between semiconductor nanoparticles and carbon nanotubes was investigated. Figure 11 shows the emission spectra of 3 + 2 ML (Figure 11a,b) and 7 + 2 ML (Figure 11c,d) thick core/shell quantum dots that are attached to MWCNTs presented. Once again, the above-mentioned blue shift is also observed in these nanocomposites. Counterintuitively, we found that the photoluminescence quenching is enhanced with an increase in the passivating ZnS shell thickness, as shown in Figure 11e−g. This is in contrast to the minimization of quenching rates that are normally observed in core/shell QDs as a function of shell thickness.[69,70] Typically, one would assume that larger shells act as a physical barrier (like longer chain ligands), and with an increased distance between an emitter and a quencher, the rates for charge transfers get more improbable as tunneling and other energy transfers (e.g., Förster resonance energy transfer (FRET)) decrease with the distance. However, such behavior for core/shell particles was observed before in the literature and attributed to prolonged lifetimes of photogenerated charge

https://doi.org/10.1021/acs.jpcc.2c01142
J. Phys. Chem. C 2022, 126, 9076−9090

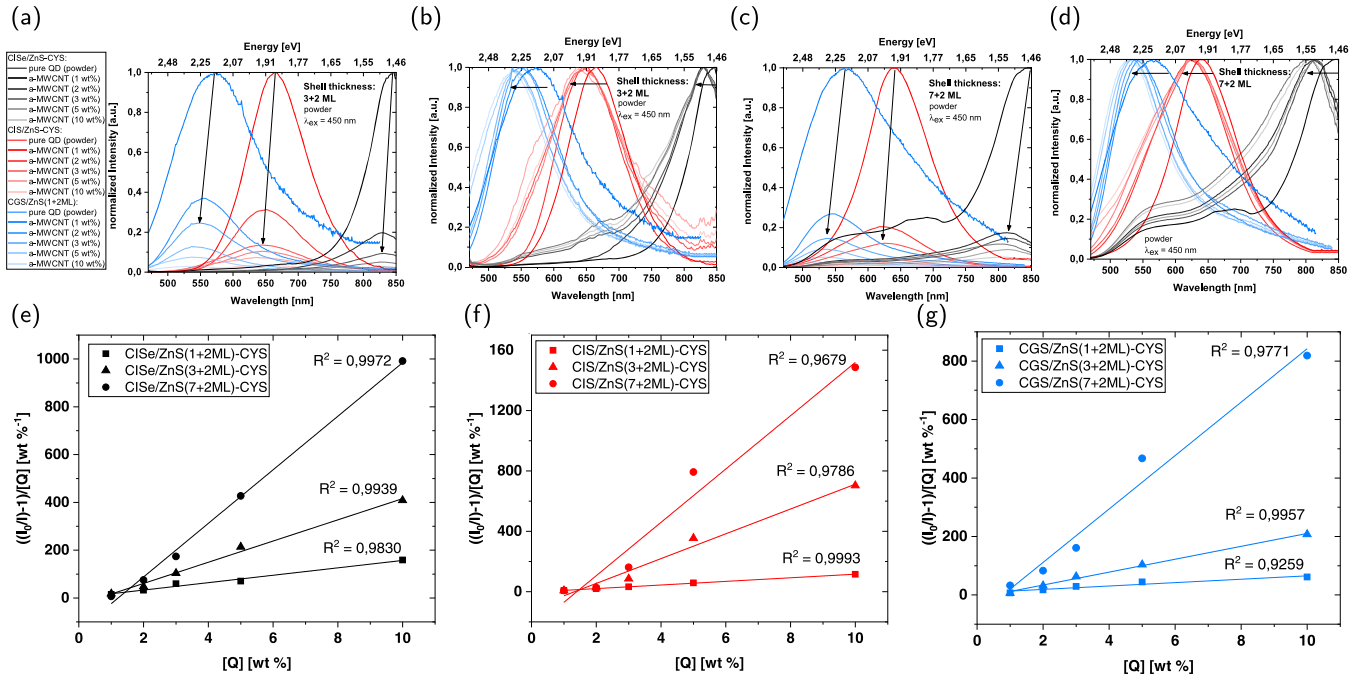

Figure 11. Normalized emission spectra of CISe, CIS, and CGS with different shell thicknesses of 3 + 2 ML (a, b) and 7 + 2 ML (c, d) of ZnS (in powder form). Comparison of the Stern−Volmer plots of CISe (e), CIS (f), and CGS (g) nanoparticles with different shell thicknesses (capped with CYS and quenched with c-MWCNT in solution).

carriers in core/shell structures with thicker shells.[71,72] Given that the Stern−Volmer constant is directly proportional to the lifetime, it appears that the enhanced probability of the quencher to diffuse toward and interact with a photoexcited emitter nanoparticle due to its long lifetime is largely responsible for the observed increased quenching rates. On top of that, it is worth mentioning that CISe/ZnS, CIS/ZnS, and CGS/ZnS are so-called type I core/shell structures, indicating that the valence band maximum (VBM) and the conduction band minimum (CBM) are lower and higher for the shell material than for the core material on a total energy scale, thus confining photogenerated electrons and holes mostly to the core region. Due to the quantum confinement effect, however, the band gap shrinks (VBM and CBM get higher and lower on a total energy scale) for larger particles. Transferred to core/shell structures with increasing shell thickness, this means that the energy barrier between the core and shell material shrinks, as it is described by Liu et al.[73] Such an effect would transform $CuInS_2$/ZnS from a type I to a quasi-type II structure upon increasing the amount of ZnS (which was confirmed via DFT calculations, see Figure S15), making charge transfer more probable.

3.4. DFT Calculations. To further investigate the influence of electric fields originating from the charged substrates onto the nanoparticles and to understand what influence the binding between QDs and CNTs has on the electronic structure of the semiconductor material, we performed DFT calculations. Since theoretical studies in the form of DFT calculations on quantum-confined QDs consisting of the investigated chalcopyrite materials are scarce and to our best knowledge no such investigations have been performed on CISe/ZnS and CGS/ZnS core/shell nanostructures, we intended to improve the accuracy of these calculations to make them as comparable to experimental results as possible. Therefore, at a relatively low computational cost, the strong on-site Coulombic interaction of localized electrons, which is insufficiently described by LDA or GGA is corrected by an additional Hubbard-like term (Hubbard U parameter). Analogous to our previous studies,[74] the values for the U parameters were obtained semiempirically (see Figure S12) and were 4.8 eV for S, 4.5 eV for Se, 9.1 eV for Zn, 6.8 eV for Cu, 8.1 eV for In, and 9.8 eV for Ga. The improvement from the standard GGA calculations toward more accurate results with GGA + U calculations is represented in the Supporting Information (see Table S2 and also see Figures S13 and S14). Figure 12a−c shows the calculated band gaps for differently sized QDs and materials as a function of the applied electrical field. The relaxed structures that were the basis of these calculations can be seen in Figures S13 and S14. The electric field was applied along the z-axis and it was simulated by adding a saw-like potential to the bare ionic potential, as implemented in the Quantum ESPRESSO package. It should be mentioned that electric fields induced by point charges, lines of charges, and planes of charges can also be simulated with the help of the Environ plug-in for Quantum ESPRESSO.[75] Since the results follow the same trend, we decided to use the computational less demanding procedure via application of the saw-like potential. When the band gaps of the different materials are compared, they follow the same trend as experimentally determined (E_g: $CuGaS_2$ > $CuInS_2$ > $CuInSe_2$). Also, the band gap increases with decreasing particle size as one would expect according to the quantum confinement effect.[76] Upon suspending the nanostructures to a positive external electric field, the band gap decreases for all materials and different sizes of the structures. For negative electric fields, the band gap increases slightly to a certain maximum after which it decreases again, and this effect is more pronounced in small structures and loses intenseness upon increasing the particle size. This observation is different from our previous studies on electric fields on ZnS QDs, and we would expect that the maximum of

https://doi.org/10.1021/acs.jpcc.2c01142
J. Phys. Chem. C 2022, 126, 9076−9090

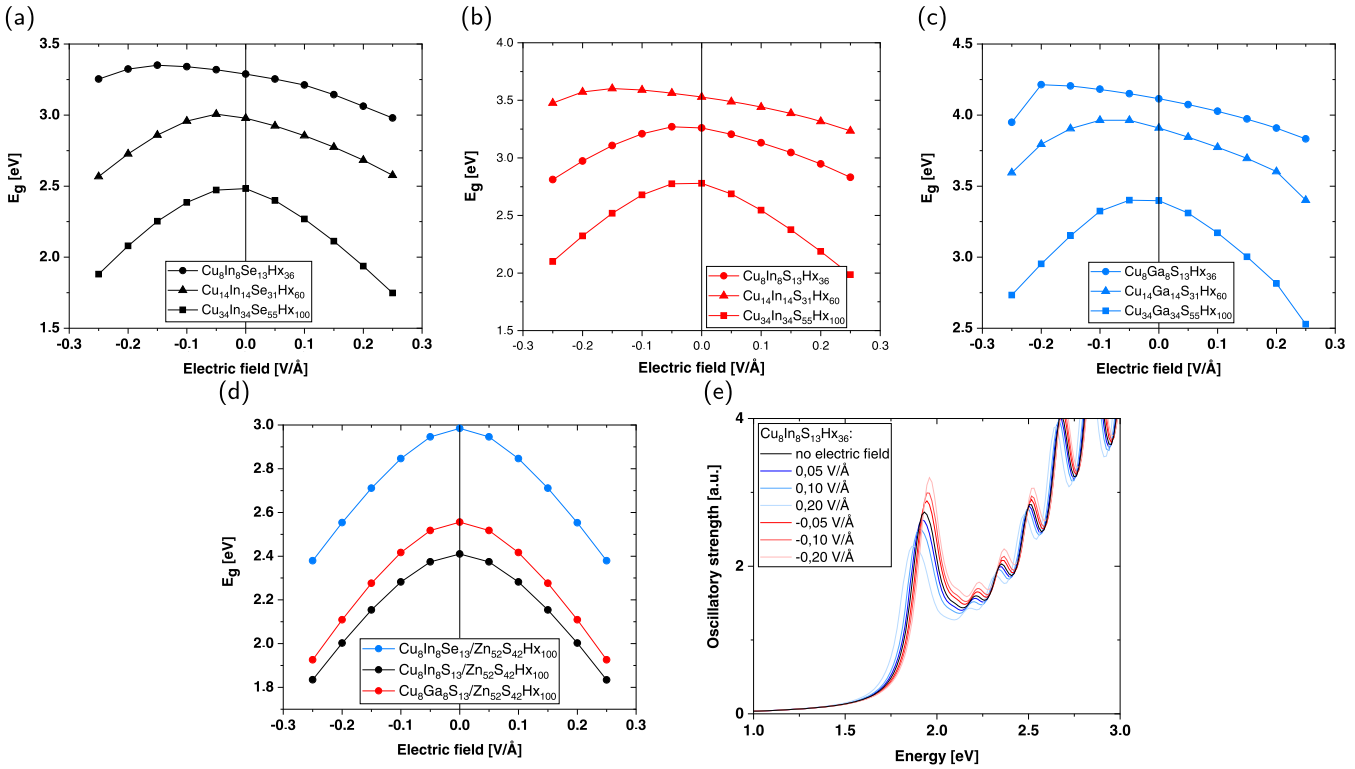

Figure 12. Electric field dependency of the band gap for different sized nanoparticles based on CISe (a), CIS (b), CGS (c), as well as core−shell/ structures (d) and calculated absorption spectra of CIS QDs subjected to different field strengths (e).

the band gap for perfectly passivated nanostructures is centered at $\vec{E}_{(z)} = 0$.[74] This however is in contrast to the computational results, which means that the surfaces of the calculated nanostructures have a nonvanishing dipole density (like in our mentioned previous studies, ZnS with surface defects). Probably this is the result of the unpreventable asymmetric distribution of surface atoms in ternary materials when two opposing surfaces are compared. This nonvanishing dipole density decreases for larger structures as the differences between two opposing surfaces also become smaller, simply due to statistical reasons, and could even be completely compensated by constructing core/shell structures with a binary material like ZnS as a shell material (see Figure 12d). Figure 12e shows the calculated absorption spectra, with and without applied electric fields, for the smallest CIS QD and basically confirms what was discussed above. It should be mentioned that the time-dependent DFT calculations (TDDFT) for the absorption spectra are performed without the Hubbard *U* correction, as this possibility is not implanted so far in the Quantum ESPRESSO package. Therefore, the energy of the first excitonic peak (which corresponds to the band-gap energy) is shifted compared to the other calculated band gaps. Nevertheless, the trend is the same. To answer the question now whether the observed blue shift is a result of the electrostatic interaction between the single components, one has to look at both theoretical and experimental results. The simulations suggest an increase of the band gap for cases with nonvanishing dipoles (like the ternary core structures or core−shell structures with surface defects) and negative applied electric fields and vice versa, a decrease of the band gap with positive electric fields. From these results alone it would be plausible to blue shift the emission wavelength by coupling quantum dots to a charged substrate. However, the simulations also suggest that this blue shift should increase upon increasing the field strength and also a red shift should be observed for an oppositely charged substrate. Experimentally, this is not what we found, as shown in Figure 10a,b; for increased surface charges of the MWCNTs, the blue shift did not increase further. Second, using oppositely charged MWCNTs, as shown in Figure 8a−d, did not result in a red shift.

Furthermore, the actual physical binding between the nanoparticles and the carbon support was also investigated, which is shown in Figure 13. Three structures are therefore simulated. First, a CIS quantum dot capped with cysteamine as a ligand (Figure 13a). Second, a c-CNT that binds via the functional $-COO^-$ group directly to the core quantum dot (Figure 13b). Third, a c-CNT where the $-COO^-$ group binds to the $-NH_3^+$ group of the cysteamine ligand (Figure 13c). No significant change in the density of states (DOS) for the nanocrystal core is observed, as shown in Figure 13d (red line corresponds to the core DOS; the influence on larger quantum dots or core/shell structures would be even smaller, thus was not considered here). This means that also other effects arising from the coupling of the binary components of the nanocomposites do not seem to have an influence on the electronic structure. Thus, we reach the conclusion that the observed change in the optical spectra is not related to induced electric fields alone. An explanation in accordance with all experimental and theoretical data would be that the blue shift is caused due to Förster resonance energy transfer (FRET). FRET is the nonradiative transfer of energy from a donor to an acceptor.[77] This energy transfer is sensitively dependent on the distance (see eq 4).

$$k_{\mathrm{FRET}} = k_{\mathrm{D}} \frac{R_0^6}{r6} \tag{4}$$

https://doi.org/10.1021/acs.jpcc.2c01142
J. Phys. Chem. C 2022, 126, 9076−9090

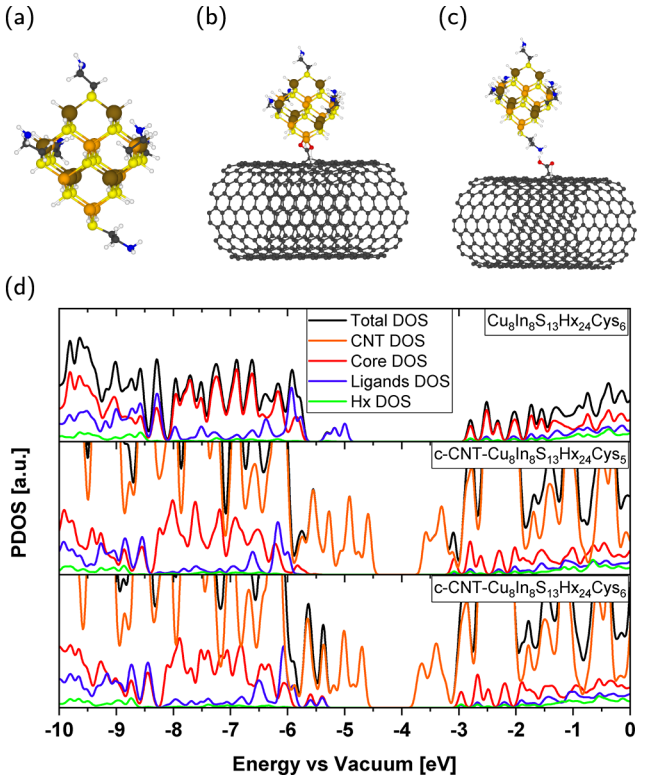

Figure 13. Relaxed structures of cysteamine-functionalized $CuInS_2$ QDs (a) and carboxylic-functionalized CNT binding to those nanostructures (orange: Cu, brown: In, yellow: S, white: Hx or H, black: C, red: O, blue: N) directly as a passivating ligand (b) or electrostatically to the amine group of the cysteamine (c) and the corresponding DOS (d).

In eq 4, k_{FRET} is the rate of the FRET, k_D is the emission rate of the donor, R_0 is the Förster distance, and r is the distance between the donor and the acceptor. In this study, in the case of the investigated solid samples (aggregated QDs), the emission wavelength was red-shifted due to a very close contact between single particles and possible energy transfer between QDs. In solution or fixed on the surface of MWCNTs, the interparticle distance is much larger (see again Figure 4c); thus, it seems reasonable that energy transfer between semiconductor nanoparticles is inhibited in these cases and therefore not red-shifted (or as we interpreted it, is observed as a blue shift). This would also explain why we do not observe this blue shift in nanocomposites formed from unstable dispersions or with the same surface charge of the single components, as the QDs agglomerate there to yield small particle distances (see again Figure 4a,b). Similar behavior was observed in the literature when QDs in their powder form were compared to QDs encapsulated in a polystyrene matrix.[78] These findings highlight once again the necessity to precisely control the aggregation behavior through surface functionalization to be able to produce nanocomposites with defined and controlled structures.

4. CONCLUSIONS

In summary, the construction of nanocomposites consisting of MWCNTs and ternary chalcogenide QDs is demonstrated via electrostatic self-assembly. Through easy and reproducible surface modification of CISe/ZnS, CIS/ZnS, and CGS/ZnS core/shell nanoparticles, together with already well-established functionalization protocols for CNTs, a toolbox for the synthesis of various heterostructures is assembled. A toolbox means access to the single components with positive or negative surface charges and the possibility to influence the magnitude of those, as well as the option to modify the structures (e.g., increase shell thicknesses or use longer chain ligands as a spacer). Thus, different variants of QDs and MWCNTs were obtained, which depending on the surface properties adjusted before were able to self-assemble into nanocomposites. We herein report the synthesis of high-quality $CuInSe_2$-, $CuInS_2$-, and $CuGaS_2$-based QDs capped with ligands like AOT and CYS and the electrostatically driven construction of nanocomposites from these together with oppositely charged MWCNTs, which to our best knowledge has not been reported before. ζ-Potential and DLS size analysis were performed to specify the surface charge and colloidal stability of the single components, which were crucial to construct nanocomposites where the nanotubes show a homogeneous surface coverage with nanocrystals. Steady-state and time-resolved photoluminescence studies were examined to investigate the quenching behavior and kinetics. During these characterizations, we found a blue shift of emission and excitation maxima, which was reported before for other nanocomposites. The origin of this shift was not well researched and there were assumptions that it could be caused by the electrostatic interaction between the binary components of the composites. From the experimental site with the established toolbox and from the theoretical site supported through DFT calculations, we were able to exclude that theory and concluded that the observed shift in energy is more likely due to FRET. Nevertheless, this change in the optical properties apart from its origin indicates a good contact between the single components, which is usually preferred in heterostructures tuned toward optoelectronic applications.

■ ASSOCIATED CONTENT

Supporting Information

The Supporting Information is available free of charge at https://pubs.acs.org/doi/10.1021/acs.jpcc.2c01142.

STEM photographs, X-ray diffraction, FTIR spectra, and emission and absorption spectra of core QDs, core/shell QDs, MWCNTs, and nanocomposites consisting of both; DFT convergence tests; semiempirical evaluation of the Hubbard U parameters; comparison between GGA, GGA + U, and experimental results for bulk and nanometer-sized semiconductor materials as well as their calculated band structures and density of states; and calculated density of states for CIS/ZnS QDs with increasing shell thickness (PDF)

■ AUTHOR INFORMATION

Corresponding Author

Dominik Voigt − *Department of Chemical Engineering, FH Münster University of Applied Sciences, 48565 Steinfurt, Germany;* orcid.org/0000-0002-5517-5604; Email: dv009200@fh-muenster.de

Authors

Giulia Primavera − *Department of Chemical Engineering, FH Münster University of Applied Sciences, 48565 Steinfurt, Germany*

https://doi.org/10.1021/acs.jpcc.2c01142
J. Phys. Chem. C 2022, 126, 9076−9090

Holger Uphoff − *Department of Physical Engineering, FH Münster University of Applied Sciences, 48565 Steinfurt, Germany*
Jan Alexander Rethmeier − *Department of Chemical Engineering, FH Münster University of Applied Sciences, 48565 Steinfurt, Germany*
Lukas Schepp − *Department of Chemical Engineering, FH Münster University of Applied Sciences, 48565 Steinfurt, Germany*
Michael Bredol − *Department of Chemical Engineering, FH Münster University of Applied Sciences, 48565 Steinfurt, Germany;* orcid.org/0000-0001-5024-2356

Complete contact information is available at: https://pubs.acs.org/10.1021/acs.jpcc.2c01142

Author Contributions

D.V. contributed to conceptualization, methodology, writing—original draft preparation, review, and editing, and visualization; G.P. contributed to methodology, visualization, and writing—original draft preparation; H.U. contributed to methodology and visualization; L.S. contributed to methodology; and J.A.R. contributed to conceptualization, supervision, and funding acquisition.

Notes

The authors declare no competing financial interest.

■ ACKNOWLEDGMENTS

This research was funded in parts by the "European Fund for Regional Development". Computational resources were generously provided by the "Campus Cluster" facility from the FH Münster University of Applied Sciences. The authors also gratefully appreciate the help of Dr. David Enseling (FH Münster University of Applied Sciences) for the instruction in measurement and evaluation of time-resolved PL spectroscopy and Daniel Dinga (FH Münster University of Applied Sciences) for the instruction in Edinburgh Spectrofluorophotometer software.

■ REFERENCES

(1) Sun, D. M.; Timmermans, M. Y.; Tian, Y.; Nasibulin, A. G.; Kauppinen, E. I.; Kishimoto, S.; Mizutani, T.; Ohno, Y. Flexible high-performance carbon nanotube integrated circuits. *Nat. Nanotechnol.* **2011**, *6*, 156−161.
(2) Prasadam, V. P.; Gautier, N.; Bahlawane, N. CNT nano-engineering for thermally stable selective solar absorption. *Mater. Today Commun.* **2021**, *28*, 102552.
(3) Marchesan, S.; Kostarelos, K.; Bianco, A.; Prato, M. The winding road for carbon nanotubes in nanomedicine. *Mater. Today* **2015**, *18*, 12−19.
(4) Park, S. H.; King, P. J.; Tian, R.; et al. High areal capacity battery electrodes enabled by segregated nanotube networks. *Nat. Energy* **2019**, *4*, 560−567.
(5) Liu, X.-M.; dong Huang, Z.; woon Oh, S.; Zhang, B.; Ma, P.-C.; Yuen, M. M.; Kim, J.-K. Carbon nanotube (CNT)-based composites as electrode material for rechargeable Li-ion batteries: A review. *Compos. Sci. Technol.* **2012**, *72*, 121−144.
(6) Yu, L.; Chen, G. Z. Redox electrode materials for supercapatteries. *J. Power Sources* **2016**, *326*, 604−612.
(7) Avouris, P.; Freitag, M.; Perebeinos, V.; et al.*et al.* Cabon-nanotube photonics and optoelectronics. *Nat. Photonics* **2008**, *2*, 341−350.
(8) Avouris, P.; Chen, J. Nanotube electronics and optoelectronics. *Mater. Today* **2006**, *9*, 46−54.
(9) Liu, Y.; Wang, S.; Liu, H.; Peng, L. M. Carbon nanotube-based three-dimensional monolithic optoelectronic integrated system. *Nat. Commun.* **2017**, *8*, No. 15649.
(10) Moisala, A.; Li, Q.; Kinloch, I.; Windle, A. Thermal and electrical conductivity of single- and multi-walled carbon nanotube-epoxy composites. *Compos. Sci. Technol.* **2006**, *66*, 1285−1288.
(11) Treacy, M. M.; Ebbesen, T. W.; Gibson, J. M. Exceptionally high Young's modulus observed for individual carbon nanotubes. *Nature* **1996**, *381*, 678−680.
(12) Bai, Y.; Zhang, R.; Ye, X.; et al. Carbon nanotube bundles with tensile strength over 80 GPa. *Nat. Nanotechnol.* **2018**, *13*, 589−595.
(13) Yin, Z.; Duoni; Chen, H.; Wang, J.; Qian, W.; Han, M.; Wei, F. Resilient, mesoporous carbon nanotube-based strips as adsorbents of dilute organics in water. *Carbon* **2018**, *132*, 329−334.
(14) Peigney, A.; Laurent, C.; Flahaut, E.; Bacsa, R. R.; Rousset, A. Specific surface area of carbon nanotubes and bundles of carbon nanotubes. *Carbon* **2001**, *39*, 507−514.
(15) Jeon, I.-Y.; Chang, D. W.; Kumar, N. A.; Baek, J.-B. In *Carbon Nanotubes*; Yellampalli, S., Ed.; IntechOpen: Rijeka, 2011; Chapter 5.
(16) Prato, M. Materials chemistry: Controlled nanotube reactions. *Nature* **2010**, *465*, 172−173.
(17) Gromov, A.; Dittmer, S.; Svensson, J.; Nerushev, O. A.; Perez-García, S. A.; Licea-Jiménez, L.; Rychwalski, R.; Campbell, E. E. Covalent amino-functionalisation of single-wall carbon nanotubes. *J. Mater. Chem.* **2005**, *15*, 3334−3339.
(18) Wu, H. C.; Chang, X.; Liu, L.; Zhao, F.; Zhao, Y. Chemistry of carbon nanotubes in biomedical applications. *J. Mater. Chem.* **2010**, *20*, 1036−1052.
(19) Balasubramanian, K.; Burghard, M. Chemically Functionalized Carbon Nanotubes. *Small* **2005**, *1*, 180−192.
(20) Syrgiannis, Z.; Melchionna, M.; Prato, M. *Encyclopedia of Polymeric Nanomaterials*; Springer Berlin Heidelberg, 2014; pp 1−8.
(21) Mehmood, U.; Ahmad, W.; Ahmed, S. Nickel impregnated multi-walled carbon nanotubes (Ni/MWCNT) as active catalyst materials for efficient and platinum-free dye-sensitized solar cells (DSSCs). *Sustainable Energy Fuels* **2019**, *3*, 3473−3480.
(22) Sadeq, Z. S.; Alshrefi, S. M.; Saleh, W. R.; Mahdi, D. K.I-V Characteristics of n-Si /ZnO/Se/MWCNTs Nanocomposite Solar Cell Fabricated by Solvothermal Technique. In *AIP Conference Proceedings*; AIP Publishing LLC, 2019; Vol. *2190*, p 020085.
(23) Vasil'eva, I. S.; Shumakovich, G. P.; Khlupova, M. E.; Vasiliev, R. B.; Emets, V. V.; Bogdanovskaya, V. A.; Morozova, O. V.; Yaropolov, A. I. Enzymatic synthesis and electrochemical characterization of sodium 1,2-naphthoquinone-4-sulfonate-doped PEDOT/MWCNT composite. *RSC Adv.* **2020**, *10*, 33010−33017.
(24) Saleh, T. A.; Gupta, V. K. Photo-catalyzed degradation of hazardous dye methyl orange by use of a composite catalyst consisting of multi-walled carbon nanotubes and titanium dioxide. *J. Colloid Interface Sci.* **2012**, *371*, 101−106.
(25) Das, S.; Sa, K.; Alam, I.; Mahanandia, P. Enhancement of photocurrent in Cu2ZnSnS4 quantum dot-anchored multi-walled carbon nanotube for solar cell application. *J. Mater. Sci.* **2019**, *54*, 8542−8555.
(26) Yu, W. J.; Liu, C.; Hou, P. X.; Zhang, L.; Shan, X. Y.; Li, F.; Cheng, H. M. Lithiation of silicon nanoparticles confined in carbon nanotubes. *ACS Nano* **2015**, *9*, 5063−5071.
(27) Yousefi, A. T.; Fukumori, M.; Reetu Raj, P.; Liu, P.; Fu, L.; Bagheri, S.; Tanaka, H. Progress on nanoparticle-based carbon nanotube complex: fabrication and potential application. *Rev. Inorg. Chem.* **2016**, *36*, 183−201.
(28) Chen, M. L.; Oh, W. C. Synthesis and highly visible-induced photocatalytic activity of CNT-CdSe composite for methylene blue solution. *Nanoscale Res. Lett.* **2011**, *6*, No. 398.
(29) Sarpong, L. K.; Bredol, M.; Schönhoff, M. Heteroaggregation of multiwalled carbon nanotubes and zinc sulfide nanoparticles. *Carbon* **2017**, *125*, 480−491.
(30) Rabouw, F. T.; de Mello Donega, C. Excited-State Dynamics in Colloidal Semiconductor Nanocrystals. *Top. Curr. Chem.* **2016**, *374*, No. 58.

(31) Guo, C.; et al. Integration of green CuInS 2 /ZnS quantum dots for high-efficiency light-emitting diodes and high-responsivity photodetectors References and links "Solution-processed PbS quantum dot infrared photodetectors and photovoltaics. *Opt. Mater. Express* **2015**, *7*, 11.
(32) Kim, J.-H.; Kim, B.-Y.; Yang, H. Synthesis of Mn-doped CuGaS_2 quantum dots and their application as single down-converters for high-color rendering solid-state lighting devices. *Opt. Mater. Express* **2018**, *8*, 221.
(33) Li, W.; Pan, Z.; Zhong, X. CuInSe2 and CuInSe2-ZnS based high efficiency "green" quantum dot sensitized solar cells. *J. Mater. Chem. A* **2015**, *3*, 1649−1655.
(34) Voigt, D.; Bredol, M.; Gonabadi, A. A general strategy for CuInS2 based quantum dots with adjustable surface chemistry. *Opt. Mater.* **2021**, *115*, 110994.
(35) Datsyuk, V.; Kalyva, M.; Papagelis, K.; Parthenios, J.; Tasis, D.; Siokou, A.; Kallitsis, I.; Galiotis, C. Chemical oxidation of multiwalled carbon nanotubes. *Carbon* **2008**, *46*, 833−840.
(36) Oytun, F.; Dizman, C.; Karatepe, N.; Alpturk, O.; Basarir, F. Preparation of transparent conducting electrode on polysulfone film via multilayer transfer of layer-by-layer assembled carbon nanotubes. *Thin Solid Films* **2017**, *625*, 168−176.
(37) Gritzner, G.; Küta, J. Recommendations on reporting electrode potentials in nonaqueous solvents: IUPC commission on electrochemistry. *Electrochim. Acta* **1984**, *29*, 869−873.
(38) Hohenberg, P.; Kohn, W. Inhomogeneous electron gas. *Phys. Rev.* **1964**, *136*, B864.
(39) Kohn, W.; Sham, L. J. Self-consistent equations including exchange and correlation effects. *Phys. Rev.* **1965**, *140*, A1133.
(40) Giannozzi, P.; Baroni, S.; Bonini, N.; et al. QUANTUM ESPRESSO: a modular and open-source software project for quantum simulations of materials. *J. Phys.: Condens. Matter* **2009**, *21*, 395502.
(41) Giannozzi, P.; Andreussi, O.; Brumme, T.; et al. Advanced capabilities for materials modelling with Quantum ESPRESSO. *J. Phys.: Condens. Matter* **2017**, *29*, 465901.
(42) Perdew, J. P.; Burke, K.; Ernzerhof, M. Generalized gradient approximation made simple. *Phys. Rev. Lett.* **1996**, *77*, 3865−3868.
(43) Cococcioni, M.; de Gironcoli, S. Linear response approach to the calculation of the effective interaction parameters in the LDA+U method. *Phys. Rev. B* **2005**, *71*, No. 035105.
(44) Tolba, S. A.; Gameel, K. M.; Ali, B. A.; Almossalami, H. A.; Allam, N. K.The DFT + U: Approaches, Accuracy, and Applications. In *Density Functional Calculations: Recent Progresses of Theory and Application*; IntechOpen, 2018.
(45) Timrov, I.; Marzari, N.; Cococcioni, M. Hubbard parameters from density-functional perturbation theory. *Phys. Rev. B* **2018**, *98*, 085127.
(46) Yu, K.; Carter, E. A. Communication: Comparing ab initio methods of obtaining effective U parameters for closed-shell materials. *J. Chem. Phys.* **2014**, *140*, 121105.
(47) Mattioli, G.; Dkhil, S. B.; Saba, M. I.; et al. Interfacial Engineering of P3HT/ZnO Hybrid Solar Cells Using Phthalocyanines: A Joint Theoretical and Experimental Investigation. *Adv. Energy Mater.* **2014**, *4*, 1301694.
(48) Khan, M. S.; Shi, L.; Zou, B. Impact of vacancy defects on optoelectronic and magnetic properties of Mn-doped ZnSe. *Comput. Mater. Sci.* **2020**, *174*, 109493.
(49) Huang, X.; Lindgren, E.; Chelikowsky, J. R. Surface passivation method for semiconductor nanostructures. *Phys. Rev. B* **2005**, *71*, No. 165328.
(50) Atieh, M. A.; Bakather, O. Y.; Al-Tawbini, B.; Bukhari, A. A.; Abuilaiwi, F. A.; Fettouhi, M. B. Effect of carboxylic functional group functionalized on carbon nanotubes surface on the removal of lead from water. *Bioinorg. Chem. Appl.* **2010**, *2010*, No. 603978.
(51) Zhang, J.; Zou, H.; Qing, Q.; Yang, Y.; Li, Q.; Liu, Z.; Guo, X.; Du, Z. Effect of chemical oxidation on the structure of single-walled carbon nanotubes. *J. Phys. Chem. B* **2003**, *107*, 3712−3718.
(52) Holzwarth, U.; Gibson, N. The Scherrer equation versus the 'Debye-Scherrer equation'. *Nat. Nanotechnol.* **2011**, *6*, 534.
(53) Alonso, M. I.; Wakita, K.; Pascual, J.; Garriga, M.; Yamamoto, N. Optical functions and electronic structure of CuInSe2, CuGaSe2, CuInS2, and CuGaS2. *Phys. Rev. B* **2001**, *63*, No. 075203.
(54) Li, L.; Pandey, A.; Werder, D. J.; Khanal, B. P.; Pietryga, J. M.; Klimov, V. I. Efficient synthesis of highly luminescent copper indium sulfide-based core/shell nanocrystals with surprisingly long-lived emission. *J. Am. Chem. Soc.* **2011**, *133*, 1176−1179.
(55) Park, J.; Kim, S. W. CuInS2/ZnS core/shell quantum dots by cation exchange and their blue-shifted photoluminescence. *J. Mater. Chem.* **2011**, *21*, 3745−3750.
(56) Sarpong, L. K.; Bredol, M.; Schönhoff, M.; Wegrzynowicz, A.; Jenewein, K.; Uphoff, H. One-pot synthesis of carbon nanotube/zinc sulfide heterostructures: Characterization and effect of electrostatic interaction on the optical properties. *Opt. Mater.* **2018**, *86*, 398−407.
(57) Kataura, H.; Kumazawa, Y.; Maniwa, Y.; Umezu, I.; Suzuki, S.; Ohtsuka, Y.; Achiba, Y. Optical properties of single-wall carbon nanotubes. *Synth. Met.* **1999**, *103*, 2555−2558.
(58) Weaver, J. E.; Dasari, M. R.; Datar, A.; Talapatra, S.; Kohli, P. Investigating photoinduced charge transfer in carbon nanotube-perylene- quantum dot hybrid nanocomposites. *ACS Nano* **2010**, *4*, 6883−6893.
(59) Stern, O. Uber die abklingungszeit der fluoreszenz. *Phys. Z.* **1919**, *20*, 183−188.
(60) Gehlen, M. H. The centenary of the Stern-Volmer equation of fluorescence quenching: From the single line plot to the SV quenching map. *J. Photochem. Photobiol., C* **2020**, *42*, 100338.
(61) Ojha, B.; Das, G. The interaction of 5-(Alkoxy)naphthalen-1-amine with bovine serum albumin and Its effect on the conformation of protein. *J. Phys. Chem. B* **2010**, *114*, 3979−3986.
(62) Pan, B.; Cui, D.; Ozkan, C. S.; et al. Effects of carbon nanotubes on photoluminescence properties of quantum dots. *J. Phys. Chem. C* **2008**, *112*, 939−944.
(63) Bansal, P.; Zhang, X.; Wang, H.; Kar, P.; Yu, W. W. Charge transfer between lead halide perovskite nanocrystals and single-walled carbon nanotubes. *Nanoscale Adv.* **2020**, *2*, 808−813.
(64) Weber, M.; Westendorf, S.; Märker, B.; Braun, K.; Scheele, M. Opportunities and challenges for electrochemistry in studying the electronic structure of nanocrystals. *Phys. Chem. Chem. Phys.* **2019**, *21*, 8992−9001.
(65) Wang, W.; Liu, G. K.; Cho, H. S.; Guo, Y.; Shi, D.; Lian, J.; Ewing, R. C. Surface charge induced Stark effect on luminescence of quantum dots conjugated on functionalized carbon nanotubes. *Chem. Phys. Lett.* **2009**, *469*, 149−152.
(66) Feng, W.; Qin, C.; Shen, Y.; Li, Y.; Luo, W.; An, H.; Feng, Y. A layer-nanostructured assembly of PbS quantum dot/multiwalled carbon nanotube for a high-performance photoswitch. *Sci. Rep.* **2014**, *4*, No. 3777.
(67) Banerjee, S.; Wong, S. S. Synthesis and Characterization of Carbon Nanotube-Nanocrystal Heterostructures. *Nano Lett.* **2002**, *2*, 195−200.
(68) Sutradhar, T.; Misra, A. The role of π-linkers and electron acceptors in tuning the nonlinear optical properties of BODIPY-based zwitterionic molecules. *RSC Adv.* **2020**, *10*, 40300−40309.
(69) Heafey, E.; Laferrière, M.; Scaiano, J. C. Comparative study of the quenching of core and core-shell CdSe quantum dots by binding and non-binding nitroxides. *Photochem. Photobiol. Sci.* **2007**, *6*, 580−584.
(70) Vinayakan, R.; Shanmugapriya, T.; Nair, P. V.; Ramamurthy, P.; Thomas, K. G. An Approach for Optimizing the Shell Thickness of Core-Shell Quantum Dots Using Photoinduced Charge Transfer. *J. Phys. Chem. C* **2007**, *111*, 10146−10149.
(71) Pálmai, M.; Kim, E. B.; Schnee, V. P.; Snee, P. T. Charge carrier pairing can impart efficient reduction efficiency to core/shell quantum dots: Applications for chemical sensing. *Nanoscale* **2020**, *12*, 23052−23060.
(72) Mir, I. A.; Das, K.; Akhter, T.; Ranjan, R.; Patel, R.; Bohidar, H. B. Eco-friendly synthesis of CuInS2 and CuInS2@ZnS quantum dots and their effect on enzyme activity of lysozyme. *RSC Adv.* **2018**, *8*, 30589−30599.

https://doi.org/10.1021/acs.jpcc.2c01142
J. Phys. Chem. C 2022, 126, 9076−9090

(73) Liu, L.; Li, H.; Liu, Z.; Xie, Y. H. The conversion of CuInS 2 /ZnS core/shell structure from type I to quasi-type II and the shell thickness-dependent solar cell performance. *J. Colloid Interface Sci.* **2019**, *546*, 276−284.
(74) Voigt, D.; Sarpong, L.; Bredol, M. Tuning the Optical Band Gap of Semiconductor Nanocomposites-A Case Study with ZnS/ Carbon. *Materials* **2020**, *13*, 4162.
(75) Andreussi, O.; Dabo, I.; Marzari, N. Revised self-consistent continuum solvation in electronic-structure calculations. *J. Chem. Phys.* **2012**, *136*, No. 064102.
(76) Takagahara, T.; Takeda, K. Theory of the quantum confinement effect on excitons in quantum dots of indirect-gap materials. *Phys. Rev. B* **1992**, *46*, 15578−15581.
(77) Deng, R.; Wang, J.; Chen, R.; Huang, W.; Liu, X. Enabling Foerster Resonance Energy Transfer from Large Nanocrystals through Energy Migration. *J. Am. Chem. Soc.* **2016**, *138*, 15972− 15979.
(78) Jung, J. Y.; Shim, Y. S.; Kim, Y. K. Improved stability of CdSeS/ ZnS quantum dots against temperature, humidity, and UV-O3 by encapsulation in crosslinked polystyrene beads. *J. Mater. Sci.* **2021**, *56*, 12315−12325.

https://doi.org/10.1021/acs.jpcc.2c01142
J. Phys. Chem. C 2022, 126, 9076−9090